Phase Behavior of TDP-43 and hnRNPH1: From Soluble and Aggregated States to Liquid-Like Droplets

Travis R Wang, Jiwu Wang

Allele Biotechnology and Pharmaceuticals, Inc., 6404 Nancy Ridge Drive, San Diego, CA 92121
The Scintillon Institute, 6868 Nancy Ridge Drive, San Diego, CA 92121

Corresponding Author:

Jiwu Wang
jiwuwang@allelebiotech.com

jiwuwang@scintillon.org

Key Words: TDP-43; hnRNPH1; Phase Separation; Intrinsically Disordered Region; low-complexity domain; SpyTag-SpyCatcher

Abstract (200 words)

Cytotoxic inclusions of TAR DNA-binding protein 43 (TDP-43) have been identified in various neurodegenerative diseases. Mediated by its low-complexity C-terminal domain (CTD), TDP-43 can undergo liquid-liquid phase separation (LLPS) and form aggregates and fibrils. These phase transitions are associated with pathological TDP-43 mislocalization and cytoplasmic aggregation. What determines whether and when TDP-43 adopts a liquid droplet state or forms solid aggregates, transiently or irreversibly? A full understanding of the underlying biophysical mechanisms will help explain the cellular toxicity of aberrant forms of TDP-43 and similar proteins, such as some of the large family of RNA-binding proteins. In this study, we generated recombinant full-length TDP-43 and maintained soluble-protein working solutions without the need of a solubility tag. By focusing on conditions that tune the electrostatic characteristics, we induced phase transitions among states of soluble TDP-43, solid aggregates, and liquid droplet phases in an expedient and controlled manner. We also obtained soluble working solutions of TDP-CTD and another crucial splicing factor, hnRNPH1, and investigated their phase behaviors as individual proteins and their interactions between each other during phase transitions. Using this system, we discovered a previously unreported aggregate-to-droplet transition and found evidence that phase separation of low-complexity domain (LCD)-containing proteins likely involves domain matching when they coaggregate out of solution.

Introduction

Protein aggregation is a defining feature of many neurodegenerative disorders, including the accumulation of amyloid-β and Tau in Alzheimer's disease, α-synuclein in Parkinson's disease, and TDP-43 in amyotrophic lateral sclerosis (ALS). A central question in ALS study is what stimuli trigger TDP-43 aggregation and which elements and properties of TDP-43 respond to the triggering stimuli. TDP-43 is a ubiquitous RNA-binding protein (RBP) that regulates RNA splicing[1], with roles in regulatory control on mRNA homeostasis, translation, transcription, and transport[2].

42 Though predominantly residing in the nucleus with an N-terminal nuclear localization signal, TDP-
43 43 shuttles between the nucleus and cytoplasm, a process found to be influenced by cellular
44 conditions such as stress[3,4]. The N-terminus region promotes self-association into dimers and
45 ordered oligomers[5], with evidence showing oligomerization into higher-order structures
46 prerequisite to elements of protein function[6,7]. Congruent to its role as an RBP, TDP-43 contains
47 two conserved RNA recognition motifs (RRMs) which mediate binding to RNA and DNA and are
48 central for TDP-43's biological roles. The C-terminus includes a low-complexity domain (LCD)
49 which is glycine-rich and aggregation-prone that regulates protein-protein interactions[8], splicing,
50 and solubility during physiological function[4,7,9].

51

52 Pathologically, the accumulation of TDP-43 aggregates is observed in 90% of cases of ALS, 50%
53 of frontotemporal lobar degeneration cases, and up to 75% in severe cases of Alzheimer's
54 disease, according to some estimates[10]. However, even in physiological functions, TDP-43 does
55 not always exist as a free soluble protein; rather, it transitions between solution and reversible
56 liquid-like droplets (LLDs) with limited mobility[3]. These droplets can change in size and shape in
57 response to cellular conditions. It appears that individual TDP-43 molecules and the oligomer
58 complexes they form exist in a constant state of flux; protein-protein interaction and aggregate
59 formation are always in play without necessarily leading to a pathological endpoint.

60

61 Under stress conditions, TDP-43 relocates to the cytoplasm to scaffold with other RBPs and RNA
62 into dynamic stress granules, which lock down translation and sequester specific molecules as a
63 coordinated cellular response to stress[11,12]. Extensive studies into stress granule composition
64 have illustrated that increased concentrations of TDP-43 lead to liquid phase separation (LLPS;
65 demixing) and depletion of native protein[13]. When forming different forms of aggregates, the
66 protein concentration and interaction strength among protein molecules are key factors that

67 modulate LLPS from a proteome-wide perspective[14]. One proposed pathway for how soluble
68 TDP-43 congregates and misfolds into toxic aggregates is through prolonged or repeated
69 homotypic-interactions at elevated concentrations within these granules, with other triggers
70 playing a role such as oxidative stress, amino acid mutation and modification, and the presence
71 of RNA[15]. However, studies using tracking and localization microscopy uncovered not only distinct
72 substructures of TDP-43 within stress granules, but also numerous regions of slow-moving TDP-
73 43 species dispersed throughout the cytoplasm, indicating TDP-43 oligomerization and
74 aggregation can also occur outside of stress granules[16,17], where protein concentrations are not
75 constrained by granule confinement. The precise mechanisms governing the dynamic balance
76 among soluble proteins, oligomer formation, and subsequent transitions into droplets and fibrillar
77 assemblies are subjects of intense study, yet remain poorly understood even with significant
78 progress made over a decade by many groups of researchers.

79 The term “aggregate” relevant to low-complexity domain (LCD)-containing RNA-binding proteins
80 commonly include oligomers that may be in the form of liquid-like droplets, hydrogel-like “glassy”
81 condensates, or solid formations of various shapes, often progressing in that order [16-18]. Stress
82 granules and similar membraneless organelles, in which most of this process has been studied,
83 dynamically organize protein–protein and protein–RNA interactions in the cytoplasm and through
84 LLPS segregate into a concentrated phase from a dilute phase. LLPS in proteins is often driven
85 by LCDs, which mediate multivalent interactions. Both full-length TDP-43 and its C-terminal
86 domain (CTD) are known to undergo phase separation in vitro[14,15].

87 Insoluble inclusions of TDP-43 proteins containing fragments of its C-terminus are a hallmark in
88 numerous neurodegenerative diseases. It is quite remarkable that nearly all pathology-relevant
89 mutations of TDP-43 reside in its CTD[8], indicating the sensitivity of CTD’s intrinsic functions to
90 any sequence perturbation despite its disordered structural morphology. This may suggest that,
91 prior to aggregation, factors beyond structural elements, such as the charges of key amino acids,

92 which can be influenced by extensive phosphorylation, acetylation, and other posttranslational
93 modifications concentrated within the region[8,19]. Additionally, charge distribution along the
94 sequence and neighboring effects, including stacking and hydrophobic interactions with specific
95 charged amino acids, may be essential for their behavior during phase transition[20]. In one report,
96 extensive mutagenesis was conducted to identify amino acid sequence as the "molecular
97 grammar" that dictates phase behavior in the Fused in Sarcoma (FUS) family[21]. In another study,
98 adjusting the placement of charged amino acids within an otherwise hydrophobic sequence
99 resulted in a twofold change in the tendency to phase-separate, without altering the net charge of
100 the polypeptide[22]. To manipulate the phase behaviors of TDP-43 through electrostatic alteration,
101 which shares many similarities with FUS, we created conditions that strongly altered the surface
102 charge of the protein and observed that it drove phase transitions into liquid droplets either directly
103 from soluble protein or, unexpectedly, through a novel reversal pathway from aggregates.
104
105 Phase separation is typically a thermodynamic process that occurs when protein-protein
106 interactions are more favourable than protein-solution interactions, separating proteins and
107 solutes into a dense phase[23]. Observed TDP-43-rich droplets in cells often contain internal
108 vacuoles filled with nucleoplasm materials, and these coexisting yet immiscible multiphase
109 occurrences correlate with ALS-causative mutations in CTD, indicating a higher-level complexity
110 of phase separation exists and is pathologically relevant[24]. Intriguingly, a reversible double-
111 emulsion structure (droplets-in-droplets) was created in vitro using Poly-rA RNA and PEG and
112 found to be due to kinetic trapping as opposed to thermodynamic equilibrium[25], but multi-phase
113 droplets have yet to be recreated with TDP-43 or other similar RNA-binding proteins in vitro in a
114 similarly controlled manner. In this report, we present our system as being able to show multi-
115 emulsion droplet formation with simple triggers and a consistent time course.
116

117 The CTD of TDP-43 has been found to form LLDs[26,27]. NMR and in vitro assays identified residue
118 321–335 of TDP-43 in the CTD region to be part of a helical core that tunes LLPS[14] whereas
119 proteolytic and cryo-EM studies identified residue 279-360 as the fibrillar core of TDP-43
120 filaments[28], encompassing the LLPS core. As for full-length TDP-43, phase separation has been
121 reported under unique poly(ADP-ribose) (PAR) binding conditions with concentrations of TDP-43
122 at 10μM[29], though in vitro LLPS of the full-length protein is still difficult to induce or control even
123 with favorable conditions such as using crowding agent PEG or aggregation-inhibiting molecules
124 dopamine and polyphenol EGCG[30,31]. Here, we present a novel system of manipulating liquid
125 phase separation of CTD and the full-length TDP-43, and for comparison, hnRNPH1. The current
126 paradigm states that TDP-43 LLPS droplets age into hydrogels, inclusions, and amyloid fibrils.
127 LLPS acts as a scaffold accelerating solid aggregate formation, often leading to direct
128 amyloidosis[30]. Our hypothesis is that the phasing-out of the soluble form starts with a "seed" area
129 in a protein-specific manner, which leads to early-stage substructural fibrils, forming solid
130 aggregates or LLDs depending on the predicted charge of this region and subsequent
131 electrostatic interactions. We further show the protein-specific seeding results by using switchable
132 combinations of fluorescent labelling schemes.
133
134 Our findings represent an unusual reversal of the conventional uni-directional liquid-to-solid
135 maturation of protein condensates, showing a more dynamic nature of the three macroscopic
136 phases of LCD-containing RNA-binding proteins, and reveal the likely role of electrostatic charge
137 in regulating LLPS.
138
139 **Results and Discussion**
140 **Multidirectional phase transitions of TDP-43 are reversible and tunable**
141 Liquid–liquid phase separation of full-length TDP-43 has been viewed as difficult to recreate in
142 vitro using recombinant proteins[32]. Several reported cases relied on an enzymatic cleavage of a

143 solubility tag to initiate aggregation, which is typically monitored by increased turbidity with the
144 enzymatic reaction difficult to control[7,33-35]. In other systems, a solution jump triggers phase
145 separation either almost instantly or very slowly—within minutes after a solution jump[29], or over 5
146 days[28]. In all cases, it has been challenging to fine-tune the process and capture time points of
147 phase transitions. To better control the transition process to gain clearer insight into the phase
148 behaviors of these proteins, we sought to generate recombinant full-length TDP-43 of sufficiently
149 high soluble concentration and stability without a large solubility tag.
150
151 The first step was to choose a method to keep TDP-43 soluble through purification. Most previous
152 attempts to produce full-length TDP-43 have relied on large solubility tags, such as GST[36], MBP[37],
153 and SUMO[15,28,31], which keep the fusion protein soluble until aggregation is triggered by enzymatic
154 tag cleavage or solution jump. Alternatively, like all proteins, recombinant TDP-43 can be readily
155 solubilized using strong denaturants such as 6-8 M urea or guanidine, with or without a solubilizing
156 tag, and this method has been employed by different investigators[29,36]. However, as complete
157 removal of these denaturants is often problematic because the protein tends to precipitate upon
158 denaturant elimination, a residual low concentration (e.g., ~0.6 M urea or guanidine) is typically
159 retained in storage buffer after purification, which may interfere with subtle aspects of phase
160 behavior. For our in vitro phase analysis system, we aimed to establish a baseline using full-
161 length TDP-43 without interference from large solubility tags or residual denaturants. We chose
162 to produce full-length TDP-43 with only a small His6-tag for purification and use urea to keep it
163 soluble during production, then refold to urea-free storage buffer. We solubilized full-length TDP-
164 43 expressed in E. coli using 6M urea that completely denatured its secondary structures without
165 affecting affinity purification via the His-tag. After washing and eluting with imidazole from cobalt
166 beads in 6 M urea-containing buffers, urea was gradually removed by stepwise dialysis against
167 buffer at 100-fold the sample volume. The urea concentration was reduced by half every 1–2
168 hours over 5-6 steps, concluding with a final exchange into urea-free buffer.

169

170 As the second step, we formulated the protein storage buffer by first testing whether high or low
171 salt conditions promote solubility. In the field of membraneless organelles and coacervates,
172 critical salt concentration is determined by the intrinsic properties such as charge-to-neutral ratio
173 among monomers of polymeric molecules such as DNA, RNA or protein, and charge distribution
174 and pattern[22,38]. Reducing the salt concentration below the critical concentration leads to energy-
175 favorable segregation of many types of proteins. This would suggest that keeping salt
176 concentration high should avoid forming aggregates during purification steps and in storage.
177 Many previous studies indeed used storage buffers containing high salt, e.g. 0.5 M NaCl or
178 KCl[28,31,36,37]. However, we found that TDP-43 tends to aggregate more under high-salt conditions
179 (e.g., 0.5 M NaCl) than under low-salt conditions (Supplementary Fig. 1a). Recent studies have
180 also reported that high salt promotes phase separation of soluble TDP-43[29,37].

181

182 The observation that high salt destabilizes the soluble state of TDP-43 suggests that charge
183 screening enhances hydrophobic and other non-ionic interactions, thereby promoting phase
184 separation. We hypothesized that similar effects could be achieved by adjusting the buffer pH
185 toward the protein's isoelectric point (pI). To test this, we prepared TDP-43 (5 μM) in a low-
186 capacity pH buffer (20 mM Tris-HCl, pH 8.0) and low salt (100 mM NaCl) and titrated the pH by
187 adding 1 M Tris-HCl at the target pH, maintaining 100 mM NaCl. Approximately 10% of the final
188 volume was required to reach the desired pH. Under these conditions, TDP-43 remained soluble
189 at pH 8.0, but the solution became turbid with diffuse assemblies at pH 7.0. At pH 6.0—near the
190 pI of full-length TDP-43—distinct solid aggregates became evident (Supplementary Fig.1b). This
191 observation is consistent with findings from the Chiti group[29], which implied that electrostatic
192 repulsion normally inhibits phase separation. Based on these results, we set the storage buffer
193 for recombinant TDP-43 as 20 mM Tris-HCl, pH 8.0, 100 mM NaCl.

194

195 By including urea during purification with a solubility-friendly storage buffer, we obtained working
196 solutions of TDP-43 suitable for phase transition analysis. A few points are noteworthy: a stepwise
197 removal of urea in our protocol enables the protein to refold through a more controlled process,
198 rather than by dropwise dilution or leaving residual denaturant[29,36]. Complete denaturation with
199 urea also eliminates the need for extensive RNA digestion followed by ion-exchange and gel-
200 filtration chromatography to remove nucleotides, which, if retained, can interfere with phase
201 separation[35].
202
203 To initiate analysis of the solution-to-aggregation transition, we altered salt concentration and pH
204 by adding 5 M NaCl and 1 M Tris-HCl (pH 6.0) to aliquots of TDP-43 (5 μM) in storage solution.
205 Once the buffer composition changes to high salt (0.5 M NaCl) at pH 6.0, TDP-43 almost
206 immediately aggregated out of solution and formed solid globules (Fig 1A). Over several hours,
207 these globules gradually assembled into larger structures composed of subunits that merged into
208 similarly disordered arrangements, reminiscent of fractal-like architectures (Fig. 1a). After 3 hours,
209 these aggregates ranged from clusters of only a few smaller congregates to assemblies spanning
210 hundreds of microns. The appearance of these structures closely resembles those described by
211 Lashuel and colleagues, which were composed of full-length TDP-43 oligomers released from
212 immobilized metal affinity chromatography only in high-imidazole (500 mM) fractions[28]. Unlike our
213 process, their assemblies required approximately five days to form. To assess whether a
214 commonly used solubility tag would alter TDP-43 phase behavior, we tested SUMO, a 101-
215 residue natural fragment with a pI of 5.2. When fused to TDP-43, the resulting construct has a pI
216 of 5.6, close to untagged TDP-43, leading us to predict that both versions would exhibit
217 comparable phase properties under our pH- and salt-based phase transition conditions. We
218 prepared a SUMO–TDP-43 fusion using the same 6 M urea denaturation and renaturation
219 protocol and observed very similar phase behavior to untagged TDP-43 (Supplementary Fig. 2a).
220 These results suggest that SUMO tagging preserves TDP-43 phase characteristics and may be

221 suitable to study phase transitions of other proteins, although pI matching should be considered.

222

223 Our findings that a change in TDP-43 net charge can modulate aggregate formation prompted us
224 to investigate whether alternative strategies for manipulating charge could similarly influence
225 TDP-43 phase behavior. The strong anionic detergent sodium dodecyl sulfate (SDS) micelles
226 facilitate denaturation of proteins and destabilization of protein complexes. The extent of
227 destabilization depends on the SDS concentration and the protein−SDS stoichiometry and the
228 resistance to 0.1-2% SDS has been used as a test of TDP-43 fibrillation strength[31,39]. Because
229 SDS introduces negative charges along the entire polypeptide, we therefore employed SDS at a
230 very low concentration, 0.03%, as a means of mildly modulating the overall protein surface
231 charge. Upon addition to TDP-43 aggregates, strikingly, the solid aggregates dispersed in the
232 field of view began to 'melt' into glassy material, but instead of dissolving and disappearing,
233 progressively transforming in shape and eventually forming round condensates, in about 6–
234 7 hours (Fig 1b). Formed droplets were quantified in circularity, roundness and solidity using
235 ImageJ quantification functions (Fig 1c). Coating aggregated TDP-43 with negative charge via
236 SDS did not dissolve the aggregates into a soluble state but instead transformed them into
237 droplets. We next asked whether introducing net negative charge to soluble TDP-43 would directly
238 induce LLPS. As shown in Fig. 1d, adding SDS to soluble TDP-43 indeed triggered droplet
239 formation, although the droplets were smaller and less dense than liquid-like formations formed
240 from aggregates. These early-phase droplets could be further enlarged and increased in
241 abundance by adding PEG8000 (Supplementary Fig. 3), a crowding agent commonly used to
242 promote LLPS[29,36]. The transitions from soluble state to solid aggregates induced by pH and salt,
243 and from soluble state or, as a novel observation, from solid aggregates to liquid-like droplets
244 upon SDS addition are schematically illustrated in Fig 1e.

245

246 The current paradigm for phase separation of LCD-containing RNA-binding proteins describes a
247 progression from soluble molecules to liquid-like condensates, then to glassy solids, and
248 ultimately to amyloid fibers[18]. It is interesting to compare the SDS-induced LLDs with LLDs formed
249 by means of adding negative net charges other than SDS. For instance, phosphomimetic
250 mutations reduced TDP-43 aggregates and increased the appearance of larger, more liquid-like
251 droplets[33]. Inside cells, phosphorylation is expected to add negative charges and there are many
252 other factors that can alter the net charge and charge distribution of proteins. McGurk *et al.*
253 reported that non-covalent binding of TDP-43 to poly(ADP-ribose) (PAR), a negatively charged
254 biopolymer and cellular regulator of protein localization and liquid demixing, promotes TDP-43
255 LLPS in vitro and is essential for its accumulation in stress granules in neurons[15]. Non-covalent
256 binding to PAR resulted in droplets comparable to those in our system using SDS, likely from
257 similar effects of adding net negative charge to TDP-43. As a matter of fact, binding to RNA would
258 add net negative charge to TDP-43 as well in normal cellular environment, which could enhance
259 LLPS according to our model along with suggestions by others[40]. Although SDS has not, to our
260 knowledge, been used as a trigger to induce LLPS in TDP-43 or other LCD-containing RNA-
261 binding proteins, it has been reported to promote LLPS of amyloid-β oligomers at
262 supraphysiological concentrations[41], suggesting its broader potential as a tool for modulating
263 phase behavior across diverse proteins. Demonstrating reversibility of solid formations with strong
264 anionic modulators could shed light on understanding TDP-43 pathology and lead to the
265 development of new therapeutic strategies.
266
267 **SDS-induced droplets possess typical liquid-like properties**
268 Three lines of evidence indicated that droplets derived from solid aggregates shown above exhibit
269 the same liquid properties as those formed by LLPS. First, these droplets fuse upon close contact
270 (Fig. 2a). Second, they dissolve in 1,6-hexanediol, similar to typical LLPS droplets (Fig. 2b).
271 Recent work has shown that glycine and other amino acids can bind phase-separating proteins

272 and modulate condensate stability and liquid-like dynamic[42], therefore, as a third test, we added
273 glycine to the droplets at 50 mM and observed pronounced changes within minutes: namely, a
274 dynamic formation of droplets-in-droplets, subsequent growth, and eventual remerging over time
275 (Fig. 2c). These dynamic changes were quantified by tracking the number of internal droplets
276 relative to the size of the encompassing outer droplets (Fig. 2d), as well as the average count of
277 droplets over a 12-minute period (Fig. 2e). Upon glycine addition, there was a rapid increase in
278 internal droplet formation, coordinated with the growth of the encompassing droplets. This was
279 followed by a consolidation phase, during which the average number of internal droplets
280 decreased. Altogether these corroborating assays provide strong evidence that the dynamic
281 liquid-like behavior of these solid-derived droplets.
282
283 When Cy5-labeled mRNA of a fluorescent protein mWasabi as biologically irrelevant mRNA was
284 allowed to bind TDP-43 prior to phase separation, the Cy5 imaging revealed that the mRNA
285 colocalized with the protein within the dense phase of the multi-emulsion droplets (Supplementary
286 Fig. 4), consistent with previous findings that full-length TDP-43 oligomers retain RNA-binding
287 capability[31]. These observations further indicate that the contents of these droplets exhibit liquid-
288 like properties similar to typical LLPS condensates, despite originating from solid assemblies
289 transformed by forced charge alteration.
290
291 **Phase transition behavior of TDP-43 can be generalized to other RNA-binding proteins.**
292 To see if any of these phase behaviors are specific to full-length TDP-43, we wanted to compare
293 TDP-43 to hnRNPH1, another nuclear RNA-binding protein that regulates alternative splicing with
294 implications in ALS and other diseases[43]. Similar to TDP-43, hnRNPH1 also has an LCD at the
295 C-terminus of the polypeptide composed of 449 residues, close to 414 in TDP-43; its pI is the
296 same at pH 6, allowing us to apply the same pH and salt conditions to manipulate the electrostatic
297 and ionic environment for phase transitions as TDP-43. We also wanted to compare the whole

298 TDP-43 protein to its aggregation-prone domain. In vivo, neuronal inclusions contain ubiquitinated
299 and phosphorylated aggregates of TDP-43 C-terminal (TDP-CTD) fragments in various sizes
300 (e.g., TDP-25 and TDP-35), created by aberrant cleavage events that contribute to ALS[44,45]. TDP-
301 CTD was initially identified as the fragment encoding amino acids 274-414 by pioneering
302 studies[14,26]. Later, 266-414[46], 267-414[27], and longer CTD 193-414 were also studied[47], and all
303 CTD segments have been found to play a major role in phase separation as well as aggregations
304 of TDP-43. The 274-414 fragment CTD has a pI close to pH 10. It is previously reported to have
305 a different phase separation response to pH gradients from the full-length[29], likely related to
306 different net charge at different pH compared to the full-length TDP-43 protein. We therefore opted
307 to study an intermediate-sized version of TDP-CTD, spanning 208 to 414 amino acids, which has
308 a predicted pI at pH 6. This allowed us to compare it to the full-length TDP-43 in parallel and
309 during protein mixing experiments.
310
311 As with full-length TDP-43, both TDP-CTD (208-414, hereby referred to as TDP-CTD in this
312 report) and hnRNPH1 formed solid assemblies when their solutions were adjusted to pH 6.0 and
313 0.5 M NaCl. Upon addition of 0.03% SDS, these assemblies transitioned into droplets, exhibiting
314 behavior broadly similar to that of full-length TDP-43 (Fig. 3a). However, the dynamics and
315 morphological details of the resulting aggregates and droplets varied among the proteins. For
316 example, TDP-CTD consistently formed larger and more compact aggregates compared to TDP-
317 43 and hnRNPH1. Whilst the primary focus of this report is to demonstrate macroscale phase
318 transition processes that can be modulated by solution conditions, further insights into the fine
319 structural differences underlying the various assembly forms of these proteins could be gained by
320 high-resolution imaging in future studies. This result nevertheless supports that the pI and high
321 salt promotion of solid aggregation and their SDS-induced conversion into droplets are not
322 specific to full-length TDP-43. This is consistent with the notion that phase behavior can be
323 dictated by a general mechanism based on electrostatic and hydrophobic interactions.

TDP-CTD droplets and aggregates are known to contain amyloid filaments[27,48,49]. To examine the amyloid nature of our TDP-43 and TDP-CTD solid aggregates, we stained them with classical amyloid-binding dyes, including thioflavin-T (ThT) and Congo Red (CR), both of which strongly fluoresce upon binding to β-sheet-rich amyloid structures. They exhibited clear and nearly uniform positive staining, suggesting that amyloid structures are present throughout the formations and likely organized at the substructural level rather than being confined to larger, assembled structures (Fig 3b). Next, we stained the droplets formed from both TDP-43 and TDP-CTD solid aggregates with SDS addition and discovered that these droplets too were remarkably ThT and CR positive (Fig 3c). Extensive studies by many groups on LLPS of TDP-CTD have shown that amyloid fibrillation can occur independently of LLPS, as observed in our solid aggregates; whereas ThT-positive amyloid fibrils have also been detected within liquid droplets, consistent with our findings in solid-derived droplets[27,50]. Although dye-staining with ThT and CR by itself is not unique to amyloids, the strong and consistent signals here nevertheless provide clear likelihood that these assemblies contain amyloid elements and justify further investigations using high-resolution imaging techniques when available for analysis of the assembly dynamics. Namely, how the helical structures present in both full-length TDP-43 and its CTD during assembly transitions can potentially give rise to β-sheet-rich structures[26,39,46].

The formation of multi-emulsion or multiphase droplets is a characteristic feature of complex coacervate (polyelectrolyte material) mixtures, which are widely viewed as models for studying charge-mediated LLPS[38]. By patterning charged monomers along a polymer backbone such as polypeptides, one can precisely adjust local charge organization and the resulting electrostatic interactions between coacervate-forming chains, creating multi-phase or multi-emulsion droplets[22]. In TDP-43, charged amino acids are naturally distributed along the polypeptide, with additional charges that can be introduced in vivo through phosphorylation and other post-

350 translational modifications, particularly concentrated in the CTD. In our in vitro phase-separation
351 system, a droplets-in-droplets morphology can be induced simply by adding glycine to SDS-
352 induced droplets (Fig 2c). As previously reported, glycine interacts weakly with amide groups in
353 the protein backbone and aromatic side chains, reducing backbone–backbone contacts while
354 enhancing interactions among aromatic residues[42]. The biological relevance lies in the surprising
355 observation that free amino acids account for more than 25% of the total volume and 6% of the
356 total dry mass of a mammalian cell[51], as well as their natural role in stabilizing proteins and
357 colloidal dispersions[52]. We set out to determine the nature of multi-emulsion droplets formed
358 following glycine addition to SDS-induced single droplets. To do this, we repeated the experiment
359 shown in Fig. 2c but in the presence of ThT, and used confocal imaging to visualize phase
360 behavior and amyloid properties. Z-stacks of representative complex droplets revealed alternating
361 dense (coacervate) and dilute (supernatant) phases within larger droplets (Fig. 3d). The 'bubbles'
362 were ThT-negative, whereas the coacervates were ThT-positive, confirming the presence of
363 amyloid substances in protein-rich coacervates at the 3D level. This result further highlights the
364 liquid-like dynamics of SDS-induced droplets and the secondary phase separation that can be
365 triggered by electrostatic effectors such as glycine.
366
367 **Amyloid formation starts upon phase separation**
368 Compared to the CTD of TDP-43, findings reported in the literature on the phase separation
369 behavior of full-length TDP-43 and the role of amyloid fibrillation are less consistent, presumably
370 due to the challenges of producing recombinant full-length TDP-43 without large solubility tags or
371 denaturing agents such as urea, even at low concentrations[32]. Among the few studies on full-
372 length TDP-43, some reported the presence of aggregates composed of proteins with disordered
373 secondary structure that failed to bind ThT[19,53,54]. Other studies observed ThT-positive segregated
374 structures, but the process required extended time, approximately 10 hours in one case[55] and 9
375 days with agitation in another[56]. Understanding this time course may provide valuable insights

376 into the fibrillation pathway, including the involvement of LLPS and solid aggregates, and is
377 essential for clarifying how disease-associated amyloid fibrils form. Leveraging the controllability
378 of aggregate and droplet formation using our solubility tag-free recombinant proteins and their
379 strong ThT staining once high order structures form, we performed fluorescence video recording
380 to capture the dynamic process of TDP-43 solutions transitioning into droplets with SDS or
381 forming solid aggregates under conditions of pH near the pI and high salt. Time-lapse images
382 extracted from videos recorded at fixed fields of view from two independent repeats show that,
383 upon addition of SDS to 0.03% at time zero, small droplets began to emerge and progressively
384 increased in size, through joining from soluble proteins or by merging with other condensates (Fig.
385 4a). Note that ThT was included in the protein solution prior to SDS addition and showed positive
386 staining in both small and large droplets at the first captured time point. While fluorescence
387 intensity increased over time, the rate of increase appeared generally in line with the growth in
388 droplet size, with a slight delay that could reflect amyloid fibrillation progressed in addition to
389 droplet growth; the total droplet counts increased during the first 4 hours before decreasing
390 through merging (Fig. 4b). A low concentration of glycine at 5mM, 10% of what was used in Fig
391 2c, was also included, and by hour 7, double-emulsion droplets shown as dark circles began to
392 appear, consistent with the results shown in Fig. 2c but at a slower pace. We then applied the
393 same video recording approach to monitor solid aggregate formation from soluble solutions.
394 Similar to SDS-induced droplet formation, aggregates triggered by pH near the isoelectric point
395 and high salt showed ThT staining shortly after the induction. These amorphous, fractal-like solids
396 continued to grow, originating entirely from recruiting soluble proteins as no merging events were
397 observed (Fig. 4c). Analysis of the area and intensity of the solid formations supports our
398 interpretation that aggregates rapidly grew from unstained protein molecules and began to
399 plateau at around 3 hours (Fig. 4d). These observations were consistent across multiple trials and
400 variations using different imaging systems, all showing a smooth transition from unstained
401 solution to clear and immediate amyloid-positive staining. This behavior contrasts with some of

402 the previous reports on full-length TDP-43, as discussed above. The discrepancy may stem from
403 our approach: our TDP-43 protein was fully denatured and then slowly renatured during
404 recombinant protein preparation, likely maintaining a more native-like conformation ready for
405 orderly assembly. Additionally, our induction was carried out by adding the triggering solution at
406 less than 10% of the final volume, creating lower perturbation or stress to the system than other
407 protocols by dropping high concentration protein solutions into low concentration buffers, perhaps
408 better reflecting biological events in vivo.
409
410 **Switchable fluorescent protein tags are a valuable tool for studying protein phase behavior**
411 We were also interested in determining whether different proteins, sharing the same or similar but
412 distinct LCDs, would co-aggregate or remain segregated upon triggering phase separation. To
413 address this, we designed a system to track multiple proteins using distinguishable fluorescent
414 labels. Because phase separation in our system depends on charges that influence electrostatic
415 and hydrophobic interactions, we avoided commonly used dyes that bind to amino acids and may
416 alter charge. Structural dyes such as ThT and CR are unsuitable for aggregate combination
417 studies because they lack protein-specific tracking capability. Instead, we adapted a switchable
418 tagging system to label TDP-43, TDP-CTD, and hnRNPH1 with spectrally distinct fluorescent
419 proteins (FPs). A 13-amino-acid SpyTag was added to the C-terminus of each protein via a 7-
420 amino-acid linker, and the 116-amino-acid SpyCatcher was fused to the N-terminus of
421 mNeonGreen[57], mScarlet3[58], and mTurquoise2[59], all of which represent FPs with optimal
422 brightness, physical and photo stability, and more stringent monomeric properties within their
423 respective spectrum to maximize fluorescence signals while minimizing aggregation artifacts (Fig.
424 5a). By briefly mixing a pair of SpyTag- and SpyCatcher-fused proteins, a fluorescent label is
425 covalently attached to the target protein via SpyTag–SpyCatcher bonding. The protein ratios
426 within each pair were optimized, with a slight excess of SpyCatcher-FP to ensure that all SpyTags
427 on target proteins were occupied (Supplementary Fig. 5).

428

429 The pI of all three SpyCatcher-FPs ranges between 5.0 and 5.5. When fused with TDP-43, TDP-
430 CTD, and hnRNPH1, the resulting fusion proteins have pIs between 5.5 and 6.0, predicting low
431 net charges like the untagged proteins under our aggregation induction conditions. As expected,
432 when the buffer was adjusted to pH 6.0 with 0.5M NaCl, the fused proteins formed solid
433 aggregates, exhibiting strong and uniform fluorescence (Fig. 5b). Each protein can be fused to
434 any FP without apparent differences in behavior when the FP was switched among the three
435 monomeric variants (Supplementary Fig. 6). We concluded that adding an FP to the C-terminus
436 of these proteins does not significantly alter their phase behavior, while it affords a convenient
437 and switchable end labeling system to study these proteins. Older versions of green and red FPs
438 have been previously used in fusions to study TDP-43 both in vivo and in vitro[37,53,60]. Our data is
439 consistent with these findings, indicating that FP tags offer reliable information about native
440 proteins. Most commonly used FPs have a slightly acidic pI, making them unlikely to interfere with
441 pH-dependent effects on net charge or electrostatic interactions of proteins with similar pIs as that
442 of TDP-43. However, caution may be warranted about the tendency of conventional avGFP-
443 derived GFP, YFP, and their variations to form weak dimers[61], particularly when they are used to
444 study oligomerization and seeding for aggregation.

445

446 With fluorescence signals appended to each protein, we performed time-lapse imaging to track
447 the transition of individual aggregates of TDP-43 and TDP-CTD that were fused to mScarlet3 and
448 mNeonGreen, respectively. Spread-out aggregates of each protein began condensing within 10
449 minutes of SDS addition and self-merged into spheroid structures within 1 hour (Fig. 5C), in
450 agreement with results shown with non-fusion TDP-43 (Fig. 1b).

451

452 **Electrostatic-driven phase separation is differential to aggregation seeding**

453 Having observed that TDP-43, its CTD, and hnRNPH1—the latter a distinct protein with

454 comparable features to TDP-43—all exhibited parallel behaviors, we explored whether phase
455 separation is directed by protein-specific features, or if it is driven by a common physical property-
456 based process, such as hydrophobic inclusion. We pairwise-mixed all three proteins, each tagged
457 with a different FP, and examined aggregates for the presence of two different proteins.
458 Interestingly, coaggregates were readily observed between full-length TDP-43 and TDP-CTD (Fig.
459 6). However, in all view areas obtained from repeated attempts, no coaggregates were detected
460 between hnRNPH1 and either TDP-43 or TDP-CTD. Because TDP-CTD is a segment of TDP-43
461 and known to be required for phase separation[24,26], we hypothesized that the cocomplex between
462 TDP-43 and TDP-CTD forms through the shared helical seed within the LLPS core previously
463 identified by biochemical and structural studies[14,28]. The LCD core sequence of hnRNPH1 differs
464 from that of TDP-43's while it is also known to be involved in phase separation[43]. These results
465 suggest that protein assembly is not driven solely by hydrophobic or other nonspecific physical
466 forces, as the process appears protein-specific. Instead, it is plausible that under conditions
467 controlling electrostatic interactions combined with hydrophobic segregation from the aqueous
468 phase, the phase separation appears mediated, or even initiated, at their LCD cores, similar to
469 the concept of "steric zipper"[62]. These flexible regions may allow transient 'kiss-and-run'
470 interactions when no matching partner is found, or bundle to form fibrils and develop amyloids
471 when matching occurs. Recently, non-canonical mechanism of protein recognition, wherein
472 transient interactions surrounding the TDP-43 conserved helical region drive the phase separation
473 of CTD through direct enhancement of site-specific, helix-mediated interactions, was illustrate as
474 an example of how the amino acid sequence can be used as a code for segregation[63]. It was
475 previously reported that the mutations within the core of 279-360 (as defined by Kumar *et al.*[28])
476 rendered TDP-43 less liquid-like[24], and led to defects in stress granule formation[64]. The sequence
477 specificity in multiple protein assembly formation revealed by our results could be useful for
478 understanding the effects of these mutations.

479

480 **Toward modulation of phase transition**

481 Based on the experimental data presented in this study, we propose a unifying perspective about
482 phase behavior of proteins such as TDP-43. Electrostatics related to charge, whether global or
483 localized, arising from natural amino acid composition and post-translational modifications is a
484 major determinant. In vitro attunement to pH, salt screen, zwitterionic glycine (and other amino
485 acids) or charge decoration by ionic detergent SDS at very low concentration, can modulate how
486 proteins like TDP-43 transition among various macroscopic phases. These manipulations can
487 induce phase transitions by shifting some microscopic substructures such as dimers, oligomers,
488 nonamyloid fibrils and amyloids to reach the lowest-energy steady state. These substructures all
489 retain a degree of fluidity and reversibility, allowing the system to respond dynamically to
490 environmental changes.

491

492 Protein assemblies can be visualized at the micron scale using optical microscopy, as shown in
493 this study, or at the nanometer scale with electron microscopy and other high-resolution
494 techniques like NMR, revealing details such as filament-containing helical amyloid core[28]. Large
495 assemblies likely originate from smaller subunits that act as building blocks, beginning as
496 oligomers and progressing through stepwise assembly. The process typically takes time,
497 occurring over hours or days[31], though notably faster in our system. These substructures may
498 share physical and chemical characteristics with the larger assemblies they form, either through
499 fractal growth into amorphous solids or by coexisting in a milieu that phase-separates into liquid-
500 like droplets. In our system, strong ThT and CR staining was observed in both solids and droplets,
501 during and after solid-to-droplet transitions with no delays, suggesting that different forms might
502 share related substructures. These staining events may originate from a seed region containing
503 an amphipathic helix shared among aggregating molecules[29], which undergo conformational
504 transitions toward increased β-sheet stacking during maturation, under stress, or with mutations,

505 as previously proposed[30,49,65]. Such seeding could allow the initial helical core and adjacent
506 sequences to act as a sorting mechanism, determining interaction partners and conditions. It is
507 important to note that RNA-binding proteins can also interact between each other as soluble
508 molecules via LCDs, such as glycine-rich regions, to perform biological functions without
509 undergoing phase transitions, as shown in our earlier in vitro protein-protein interaction
510 studies[66,67].
511
512
513 TDP-43 is known to co-segregate under physiological conditions with numerous other proteins,
514 including hnRNPA1, hnRNPA2, and FUS[3,68,69], through domain-specific physical contact, via RNA
515 binding, or perhaps coaggregation based on matching helix or β-sheet stacking at seed region.
516 The phase transitions observed here with TDP-43 and hnRNPH1 may extend beyond RNA-
517 binding proteins involved in splicing regulation. A notable early example is Sear's 2007 prediction
518 that the Dvl protein would undergo LLPS[70], an all-or-none switch that has since been shown to
519 play a critical role in the Wnt signaling pathway[71].
520
521 The discovery that solid aggregates can be driven into a more liquid-like state may open new
522 avenues for identifying therapeutic intervention points by preserving normal, reversible LLPS that
523 does not progress to irreversible fibril amyloid formation[72]. Potential strategies include using short
524 RNAs to provide specificity by targeting RNA-binding proteins, and amino acids or oligopeptides
525 to achieve charge-modifying effects.
526
527 **Materials and Methods**
528 **Protein production**
529 Plasmids encoding TDP-43, TDP-CTD, hnRNPH1, and SUMO–TDP-43 were cloned into the
530 pNCS vector[57] and transformed into NEB SHuffle E. coli competent cells. Selected colonies were

531 inoculated into culture tubes containing 5mL 0.1 mg/mL carbenicillin 2xYT broth and incubated at
532 30°C overnight while shaking, the next day transferred to 500mL 2xYT broth and again incubated
533 overnight while shaking. For expression, small cultures of transformed bacteria were inoculated
534 in 500 mL 2×YT broth supplemented with 0.1 mg/mL carbenicillin at 30°C while shaking overnight.
535 Cells were harvested by centrifugation at 8,000 × g, and the pellets were resuspended in lysis
536 buffer containing 20 mM Tris-HCl (pH 8.0), 6 M urea, 500 mM NaCl, and 10 mM imidazole.
537
538 Cells were lysed by sonication on ice (30% amplitude, 5 min total, 10 s on/10 s off) and centrifuged
539 at 8,000 × g to remove debris. The supernatant was incubated at 4 °C for 1 h to overnight with
540 nickel beads to capture His-tagged proteins. Bead–protein complexes were transferred to
541 purification columns and washed 3–4 times with wash buffer (20 mM Tris-HCl, pH 8.0; 500 mM
542 NaCl; 10 mM imidazole; 6 M urea). Proteins were eluted in a single step using elution buffer (20
543 mM Tris-HCl, pH 8.0; 500 mM NaCl; 200 mM imidazole; 4.5 M urea) and filtered through 0.22 μm
544 PES syringe filters.
545
546 Protein purity was assessed by SDS-PAGE, and concentrations were measured using NanoDrop.
547 Eluted proteins were standardized to 5 μM, or about 0.2 mg/ml, after removal of urea in gradual
548 5-6 step dialysis using Spectra/Por dialysis tubing (MW cutoff 7,000) against storage buffer of 20
549 mM Tris-HCl, pH 8.0 100 mM NaCl with urea concentration decreasing ~50% per step until all
550 urea was removed. Soluble proteins were collected and stored at −20 °C.
551
552 **Formation of solid aggregates**
553 Phase separation reactions for TDP-43, TDP-CTD, and hnRNPH1 were initiated from soluble
554 protein fractions by adjusting the storage buffer from pH 8 to pH 6 using small-volume additions
555 of 1 M Tris-HCl pH buffer. Additional modifications, such as changes in salt concentration, were
556 made by adding small volumes of high-molar salt solutions. The total reaction volume was

557 approximately 40 μL. All added reagents to modify experimental conditions resulted in <10%
558 increase to the total reaction volume. Aggregates from all proteins were monitored at designated
559 time points, with complete formation typically occurring within 5 hours.
560
561 **Formation of liquid-like condensates**
562 Liquid-like condensates were generated from either soluble proteins or pre-formed solid
563 aggregates by adding 1% SDS directly to the reaction mixture. The transition typically completed
564 within 8 hours. The final SDS concentration was 0.03%, consistent across all stated methods.
565
566 In experiments where glycine was added to probe the effects of addition, the final concentration
567 of glycine was 50 mM for experiments shown in Fig. 2c, and 5mM in Fig. 4a. Concentrated glycine
568 was diluted directly to the experimental conditions.
569
570 To quantify droplet shape characteristics, three geometric descriptors were calculated from binary
571 images: circularity, roundness, and solidity.
572 Circularity was calculated using the formula:
573 $\text{Circularity} = (4 \times \pi \times \text{Area}) / (\text{Perimeter}^2)$
574 This metric ranges from 0 to 1, where a value of 1 indicates a perfect circle. Lower values suggest
575 more elongated or irregular shapes.
576
577 Roundness was defined as:
578 $\text{Roundness} = (4 \times \text{Area}) / (\pi \times (\text{Major Axis Length})^2)$
579 Roundness also ranges from 0 to 1, with higher values indicating shapes closer to a perfect circle,
580 but it is more sensitive to elongation than circularity.
581
582 Solidity was computed as:

583 Solidity = Area / Convex Hull Area

584 Solidity measures the extent to which a shape is convex. A value of 1 indicates a completely
585 convex shape, while lower values suggest the presence of concavities or irregular boundaries.
586 All measurements were performed using image analysis software capable of extracting shape
587 descriptors from segmented droplet images.

588

589 **Imaging**

590 Microscopy imaging included bright field, phase contrast, widefield fluorescence, and confocal
591 fluorescence modalities. The primary instrument was the Keyence BZ-X800 fluorescence
592 microscope for both light and fluorescence imaging. Additional bright-field and widefield
593 fluorescence images were captured using the EVOS FL Fluorescence Digital Microscope, while
594 confocal fluorescence imaging was performed with the BioTek Cytation C10 Confocal Imaging
595 Reader. Images taken by Cytation C10 were at 40x magnification. All other images were taken at
596 20x magnification.

597

598 **Image analysis and quantifications**

599 Image contrast and brightness were adjusted uniformly for clarity using ImageJ. Quantitative
600 measurements were also performed using ImageJ's built-in analysis functions.

601

602 For quantifications of fluorescence images, ImageJ's color threshold function was used to
603 delineate positive signals from background signal. The analysis function provided a count of
604 detected structure, the area covered by structures of the total visible area Area%, as well as
605 fluorescence intensity IntDen.

606

607 IntDen or Integrated Density is the product of mean gray value (a stand-in for intensity) and area,
608 representing the amount of dye bound and fluorescing. The units are (relative fluorescence units)

609 * (μm^2). Corrected Total View Fluorescence is used to represent the intensity of fluorescence in
610 our measurements, which takes the IntDen value from each measured object and corrects for
611 background fluorescence. The equation is as follows:
612 CTFV = IntDen – (Area of Droplet * Mean fluorescence of background)
613
614 The mean fluorescence of background was measured by averaging 3 separate readings of the
615 background for each time point and view of the well.
616
617 **Dye staining**
618 Protein assemblies were stained by incubating at room temperature for 2–3 hours with Thioflavin
619 T (ThT) or Congo Red (CR) from Sigma. Final concentrations in wells were 40 μM ThT or 0.5%
620 CR. For time course experiments shown in Fig. 4, ThT was added to the solution before the phase
621 separation was induced.
622
623 **SpyTag/SpyCatcher Conjugation**
624 Protein constructs were conjugated by incubating together at room temperature for 1 hour. FP–
625 SpyCatcher was added in slight excess (10%) over TDP/CTD/hnRNPH1–SpyTag to achieve a
626 1.1:1 molar ratio. For quenching, excess SpyTag-tagged nanobodies (at least 4× the molarity of
627 SpyCatcher–FP) were added to bind any remaining free SpyCatcher–FP, followed by an
628 additional 1-hour incubation at room temperature.
629
630 **Acknowledgment**
631 We thank Alex Ward for some of the initial DNA constructions and initial attempts at protein
632 production, Andrew Chammas and Nathan Shaner for help with designing of SpyTag and
633 SpyCatcher constructs, Aryan Mudliar for lab assistance and discussions.
634

635 **Author Contributions**

636 JW conceptually initiated the project; TRW designed and carried out the experiments; TRW and
637 JW interpreted data and drafted the manuscript.

638

639 **Competing Interest**

640 JW is a current employee of Allele Biotech, a biotech company in the US.

641

642 **Data Availability**

643 Additional, related data of the present report is available from the corresponding author upon
644 reasonable request.

645

646 **Supplementary Material**

647 Supplementary material.doc: Supplementary figures, materials and methods

648

649 **References**

650 1 Polymenidou, M. *et al.* Long pre-mRNA depletion and RNA missplicing contribute to
651 neuronal vulnerability from loss of TDP-43. *Nat Neurosci* **14**, 459-468 (2011).
652 https://doi.org/10.1038/nn.2779
653 2 Ishiguro, T. *et al.* Regulatory Role of RNA Chaperone TDP-43 for RNA Misfolding and
654 Repeat-Associated Translation in SCA31. *Neuron* **94**, 108-124 e107 (2017).
655 https://doi.org/10.1016/j.neuron.2017.02.046
656 3 Gasset-Rosa, F. *et al.* Cytoplasmic TDP-43 De-mixing Independent of Stress Granules
657 Drives Inhibition of Nuclear Import, Loss of Nuclear TDP-43, and Cell Death. *Neuron* **102**,
658 339-357 e337 (2019). https://doi.org/10.1016/j.neuron.2019.02.038
659 4 Ayala, Y. M. *et al.* Structural determinants of the cellular localization and shuttling of TDP-
660 43. *J Cell Sci* **121**, 3778-3785 (2008). https://doi.org/10.1242/jcs.038950
661 5 Shiina, Y., Arima, K., Tabunoki, H. & Satoh, J. TDP-43 dimerizes in human cells in culture.
662 *Cell Mol Neurobiol* **30**, 641-652 (2010). https://doi.org/10.1007/s10571-009-9489-9
663 6 Perez-Berlanga, M. *et al.* Loss of TDP-43 oligomerization or RNA binding elicits distinct
664 aggregation patterns. *EMBO J* **42**, e111719 (2023).
665 https://doi.org/10.15252/embj.2022111719

666 7 Wang, A. *et al.* A single N-terminal phosphomimic disrupts TDP-43 polymerization, phase
667 separation, and RNA splicing. *EMBO J* **37** (2018).
668 https://doi.org/10.15252/embj.201797452
669 8 Santamaria, N., Alhothali, M., Alfonso, M. H., Breydo, L. & Uversky, V. N. Intrinsic disorder
670 in proteins involved in amyotrophic lateral sclerosis. *Cell Mol Life Sci* **74**, 1297-1318
671 (2017). https://doi.org/10.1007/s00018-016-2416-6
672 9 Buratti, E. *et al.* TDP-43 binds heterogeneous nuclear ribonucleoprotein A/B through its
673 C-terminal tail: an important region for the inhibition of cystic fibrosis transmembrane
674 conductance regulator exon 9 splicing. *J Biol Chem* **280**, 37572-37584 (2005).
675 https://doi.org/10.1074/jbc.M505557200
676 10 Jo, M. *et al.* The role of TDP-43 propagation in neurodegenerative diseases: integrating
677 insights from clinical and experimental studies. *Exp Mol Med* **52**, 1652-1662 (2020).
678 https://doi.org/10.1038/s12276-020-00513-7
679 11 Lang, R., Hodgson, R. E. & Shelkovnikova, T. A. TDP-43 in nuclear condensates: where,
680 how, and why. *Biochem Soc Trans* **52**, 1809-1825 (2024).
681 https://doi.org/10.1042/BST20231447
682 12 Lee, Y. B. *et al.* Cytoplasmic TDP-43 is involved in cell fate during stress recovery. *Hum Mol*
683 *Genet* **31**, 166-175 (2021). https://doi.org/10.1093/hmg/ddab227
684 13 Chen, Y. & Cohen, T. J. Aggregation of the nucleic acid-binding protein TDP-43 occurs via
685 distinct routes that are coordinated with stress granule formation. *J Biol Chem* **294**, 3696-
686 3706 (2019). https://doi.org/10.1074/jbc.RA118.006351
687 14 Conicella, A. E. *et al.* TDP-43 alpha-helical structure tunes liquid-liquid phase separation
688 and function. *Proc Natl Acad Sci U S A* **117**, 5883-5894 (2020).
689 https://doi.org/10.1073/pnas.1912055117
690 15 McGurk, L. *et al.* Poly(ADP-Ribose) Prevents Pathological Phase Separation of TDP-43 by
691 Promoting Liquid Demixing and Stress Granule Localization. *Mol Cell* **71**, 703-717 e709
692 (2018). https://doi.org/10.1016/j.molcel.2018.07.002
693 16 Fonda, B. D., Jami, K. M., Boulos, N. R. & Murray, D. T. Identification of the Rigid Core for
694 Aged Liquid Droplets of an RNA-Binding Protein Low Complexity Domain. *Journal of the*
695 *American Chemical Society* **143**, 6657-6668 (2021). https://doi.org/10.1021/jacs.1c02424
696 17 Lin, Y., Protter, D. S., Rosen, M. K. & Parker, R. Formation and Maturation of Phase-
697 Separated Liquid Droplets by RNA-Binding Proteins. *Mol Cell* **60**, 208-219 (2015).
698 https://doi.org/10.1016/j.molcel.2015.08.018
699 18 Shin, Y. & Brangwynne, C. P. Liquid phase condensation in cell physiology and disease.
700 *Science* **357** (2017). https://doi.org/10.1126/science.aaf4382
701 19 Johnson, B. S. *et al.* TDP-43 is intrinsically aggregation-prone, and amyotrophic lateral
702 sclerosis-linked mutations accelerate aggregation and increase toxicity. *J Biol Chem* **284**,
703 20329-20339 (2009). https://doi.org/10.1074/jbc.M109.010264
704 20 François-Moutal, L. *et al.* Structural Insights Into TDP-43 and Effects of Post-translational
705 Modifications. *Frontiers in Molecular Neuroscience* **12** (2019).
706 https://doi.org/10.3389/fnmol.2019.00301
707 21 Wang, J. *et al.* A Molecular Grammar Governing the Driving Forces for Phase Separation
708 of Prion-like RNA Binding Proteins. *Cell* **174**, 688-699 e616 (2018).
709 https://doi.org/10.1016/j.cell.2018.06.006

710 22 Chang, L. W. *et al.* Sequence and entropy-based control of complex coacervates. *Nat*
711 *Commun* **8**, 1273 (2017). https://doi.org/10.1038/s41467-017-01249-1
712 23 Millar, S. R. *et al.* A New Phase of Networking: The Molecular Composition and Regulatory
713 Dynamics of Mammalian Stress Granules. *Chem Rev* **123**, 9036-9064 (2023).
714 https://doi.org/10.1021/acs.chemrev.2c00608
715 24 Schmidt, H. B. & Rohatgi, R. In Vivo Formation of Vacuolated Multi-phase Compartments
716 Lacking Membranes. *Cell Rep* **16**, 1228-1236 (2016).
717 https://doi.org/10.1016/j.celrep.2016.06.088
718 25 Erkamp, N. A. *et al.* Spatially non-uniform condensates emerge from dynamically arrested
719 phase separation. *Nature Communications* **14** (2023). https://doi.org/10.1038/s41467-
720 023-36059-1
721 26 Conicella, A. E., Zerze, G. H., Mittal, J. & Fawzi, N. L. ALS Mutations Disrupt Phase
722 Separation Mediated by alpha-Helical Structure in the TDP-43 Low-Complexity C-Terminal
723 Domain. *Structure* **24**, 1537-1549 (2016). https://doi.org/10.1016/j.str.2016.07.007
724 27 Babinchak, W. M. *et al.* The role of liquid-liquid phase separation in aggregation of the
725 TDP-43 low-complexity domain. *J Biol Chem* **294**, 6306-6317 (2019).
726 https://doi.org/10.1074/jbc.RA118.007222
727 28 Kumar, S. T. *et al.* Seeding the aggregation of TDP-43 requires post-fibrillization
728 proteolytic cleavage. *Nature Neuroscience* **26**, 983-996 (2023).
729 https://doi.org/10.1038/s41593-023-01341-4
730 29 Staderini, T., Bigi, A., Mongiello, D., Cecchi, C. & Chiti, F. Biophysical characterization of
731 full-length TAR DNA-binding protein (TDP-43) phase separation—solution-jump. *Protein*
732 *Sci* **31**, e4509 (2022). https://doi.org/10.1002/pro.4509
733 30 Liu, Y. *et al.* The Regulation of TDP-43 Structure and Phase Transitions: A Review. *Protein*
734 *J* **44**, 113-132 (2025). https://doi.org/10.1007/s10930-025-10261-0
735 31 Yang, L., Jasiqi, Y. & Lashuel, H. Recombinant Full-Length TDP-43 Oligomers Retain Their
736 Ability to Bind RNAs, Are Not Toxic, and Do Not Seed TDP-43 Aggregation in Vitro. *ACS*
737 *Chem Neurosci* **15**, 193-204 (2024). https://doi.org/10.1021/acschemneuro.3c00691
738 32 Staderini, T. *et al.* Biophysical characterization of the phase separation of TDP-43 devoid
739 of the C-terminal domain. *Cell Mol Biol Lett* **29**, 104 (2024).
740 https://doi.org/10.1186/s11658-024-00615-4
741 33 Gruijs Da Silva, L. A. *et al.* Disease‐linked TDP‐43 hyperphosphorylation suppresses
742 TDP‐43 condensation and aggregation. *The EMBO Journal* **41** (2022).
743 https://doi.org/10.15252/embj.2021108443
744 34 Mann, J. R. *et al.* RNA Binding Antagonizes Neurotoxic Phase Transitions of TDP-43.
745 *Neuron* **102**, 321-338 e328 (2019). https://doi.org/10.1016/j.neuron.2019.01.048
746 35 Molliex, A. *et al.* Phase separation by low complexity domains promotes stress granule
747 assembly and drives pathological fibrillization. *Cell* **163**, 123-133 (2015).
748 https://doi.org/10.1016/j.cell.2015.09.015
749 36 Vivoli Vega, M. *et al.* Isolation and characterization of soluble human full-length TDP-43
750 associated with neurodegeneration. *FASEB J* **33**, 10780-10793 (2019).
751 https://doi.org/10.1096/fj.201900474R

752 37 Krainer, G. *et al.* Reentrant liquid condensate phase of proteins is stabilized by
753 hydrophobic and non-ionic interactions. *Nature Communications* **12** (2021).
754 https://doi.org/10.1038/s41467-021-21181-9
755 38 Lu, T. & Spruijt, E. Multiphase Complex Coacervate Droplets. *J Am Chem Soc* **142**, 2905-
756 2914 (2020). https://doi.org/10.1021/jacs.9b11468
757 39 Garg, D. K. & Bhat, R. Modulation of assembly of TDP-43 low-complexity domain by
758 heparin: From droplets to amyloid fibrils. *Biophysical Journal* **121**, 2568-2582 (2022).
759 https://doi.org/10.1016/j.bpj.2022.05.042
760 40 Wang, C. *et al.* Stress Induces Dynamic, Cytotoxicity-Antagonizing TDP-43 Nuclear Bodies
761 via Paraspeckle LncRNA NEAT1-Mediated Liquid-Liquid Phase Separation. *Mol Cell* **79**,
762 443-458 e447 (2020). https://doi.org/10.1016/j.molcel.2020.06.019
763 41 Gui, X. *et al.* Liquid-liquid phase separation of amyloid-beta oligomers modulates amyloid
764 fibrils formation. *J Biol Chem* **299**, 102926 (2023).
765 https://doi.org/10.1016/j.jbc.2023.102926
766 42 Xu, X. *et al.* Amino acids bind to phase-separating proteins and modulate biomolecular
767 condensate stability and dynamics. *Nature Communications* **16** (2025).
768 https://doi.org/10.1038/s41467-025-63755-x
769 43 Kim, G. H. & Kwon, I. Distinct roles of hnRNPH1 low-complexity domains in splicing and
770 transcription. *Proc Natl Acad Sci U S A* **118** (2021).
771 https://doi.org/10.1073/pnas.2109668118
772 44 Neumann, M. *et al.* Ubiquitinated TDP-43 in frontotemporal lobar degeneration and
773 amyotrophic lateral sclerosis. *Science* **314**, 130-133 (2006).
774 https://doi.org/10.1126/science.1134108
775 45 Zhang, Y. J. *et al.* Aberrant cleavage of TDP-43 enhances aggregation and cellular toxicity.
776 *Proc Natl Acad Sci U S A* **106**, 7607-7612 (2009).
777 https://doi.org/10.1073/pnas.0900688106
778 46 Li, H. R. *et al.* The physical forces mediating self-association and phase-separation in the
779 C-terminal domain of TDP-43. *Biochim Biophys Acta Proteins Proteom* **1866**, 214-223
780 (2018). https://doi.org/10.1016/j.bbapap.2017.10.001
781 47 Prasad, A., Sivalingam, V., Bharathi, V., Girdhar, A. & Patel, B. K. The amyloidogenicity of
782 a C-terminal region of TDP-43 implicated in Amyotrophic Lateral Sclerosis can be affected
783 by anions, acetylation and homodimerization. *Biochimie* **150**, 76-87 (2018).
784 https://doi.org/10.1016/j.biochi.2018.05.003
785 48 Guo, W. *et al.* An ALS-associated mutation affecting TDP-43 enhances protein
786 aggregation, fibril formation and neurotoxicity. *Nat Struct Mol Biol* **18**, 822-830 (2011).
787 https://doi.org/10.1038/nsmb.2053
788 49 Jiang, L.-L. *et al.* Structural Transformation of the Amyloidogenic Core Region of TDP-43
789 Protein Initiates Its Aggregation and Cytoplasmic Inclusion. *Journal of Biological Chemistry*
790 **288**, 19614-19624 (2013). https://doi.org/10.1074/jbc.m113.463828
791 50 Pakravan, D. *et al.* Liquid-Liquid Phase Separation Enhances TDP-43 LCD Aggregation but
792 Delays Seeded Aggregation. *Biomolecules* **11** (2021).
793 https://doi.org/10.3390/biom11040548
794 51 Rollin, R., Joanny, J. F. & Sens, P. Physical basis of the cell size scaling laws. *Elife* **12** (2023).
795 https://doi.org/10.7554/eLife.82490

52 Mao, T. *et al.* Stabilizing effect of amino acids on protein and colloidal dispersions. *Nature* **645**, 915-921 (2025). https://doi.org/10.1038/s41586-025-09506-w

53 Sun, Y. *et al.* Physiologically Important Electrolytes as Regulators of TDP-43 Aggregation and Droplet-Phase Behavior. *Biochemistry* **58**, 590-607 (2019). https://doi.org/10.1021/acs.biochem.8b00842

54 Capitini, C. *et al.* Full-length TDP-43 and its C-terminal domain form filaments in vitro having non-amyloid properties. *Amyloid* **28**, 56-65 (2021). https://doi.org/10.1080/13506129.2020.1826425

55 Lin, P. H. *et al.* TDP-43 Amyloid Fibril Formation via Phase Separation-Related and -Unrelated Pathways. *ACS Chem Neurosci* **15**, 3767-3775 (2024). https://doi.org/10.1021/acschemneuro.4c00503

56 Esposto, J. C. & Martic, S. Phosphorylated TAR DNA-binding protein-43: Aggregation and antibody-based inhibition. *Biochim Biophys Acta Mol Basis Dis* **1867**, 166234 (2021). https://doi.org/10.1016/j.bbadis.2021.166234

57 Shaner, N. C. *et al.* A bright monomeric green fluorescent protein derived from Branchiostoma lanceolatum. *Nature Methods* **10**, 407-409 (2013).

58 Gadella, T. W. J., Jr. *et al.* mScarlet3: a brilliant and fast-maturing red fluorescent protein. *Nat Methods* **20**, 541-545 (2023). https://doi.org/10.1038/s41592-023-01809-y

59 Goedhart, J. *et al.* Structure-guided evolution of cyan fluorescent proteins towards a quantum yield of 93%. *Nat Commun* **3**, 751 (2012). https://doi.org/10.1038/ncomms1738

60 Schmidt, H. B., Barreau, A. & Rohatgi, R. Phase separation-deficient TDP43 remains functional in splicing. *Nat Commun* **10**, 4890 (2019). https://doi.org/10.1038/s41467-019-12740-2

61 Nakagawa, C., Nishimura, S., Senda-Murata, K. & Sugimoto, K. A rapid and simple method of evaluating the dimeric tendency of fluorescent proteins in living cells using a truncated protein of importin alpha as fusion tag. *Biosci Biotechnol Biochem* **76**, 388-390 (2012). https://doi.org/10.1271/bbb.110677

62 Sawaya, M. R., Hughes, M. P., Rodriguez, J. A., Riek, R. & Eisenberg, D. S. The expanding amyloid family: Structure, stability, function, and pathogenesis. *Cell* **184**, 4857-4873 (2021). https://doi.org/10.1016/j.cell.2021.08.013

63 Mohanty, P. *et al.* A synergy between site-specific and transient interactions drives the phase separation of a disordered, low-complexity domain. *Proc Natl Acad Sci U S A* **120**, e2305625120 (2023). https://doi.org/10.1073/pnas.2305625120

64 Dubinski, A. *et al.* Stress granule assemblyin vivois deficient in the CNS of mutant TDP-43 ALS mice. *Human Molecular Genetics* **32**, 319-332 (2023). https://doi.org/10.1093/hmg/ddac206

65 Yan, X. *et al.* Intra-condensate demixing of TDP-43 inside stress granules generates pathological aggregates. *Cell* **188**, 4123-4140 e4118 (2025). https://doi.org/10.1016/j.cell.2025.04.039

66 Wang, J. & Bell, L. R. The Sex-lethal amino terminus mediates cooperative interactions in RNA binding and is essential for splicing regulation. *Genes Dev* **8**, 2072-2085 (1994). https://doi.org/10.1101/gad.8.17.2072

838 67 Wang, J., Dong, Z. & Bell, L. R. Sex-lethal interactions with protein and RNA. Roles of
839 glycine-rich and RNA binding domains. *J Biol Chem* **272**, 22227-22235 (1997).
840 https://doi.org/10.1074/jbc.272.35.22227
841 68 Ryan, V. H. *et al.* Mechanistic View of hnRNPA2 Low-Complexity Domain Structure,
842 Interactions, and Phase Separation Altered by Mutation and Arginine Methylation. *Mol*
843 *Cell* **69**, 465-479 e467 (2018). https://doi.org/10.1016/j.molcel.2017.12.022
844 69 Freibaum, B. D., Chitta, R. K., High, A. A. & Taylor, J. P. Global analysis of TDP-43 interacting
845 proteins reveals strong association with RNA splicing and translation machinery. *J*
846 *Proteome Res* **9**, 1104-1120 (2010). https://doi.org/10.1021/pr901076y
847 70 Sear, R. P. Dishevelled: a protein that functions in living cells by phase separating. *Soft*
848 *Matter* **3**, 680-684 (2007). https://doi.org/10.1039/b618126k
849 71 Kang, K., Shi, Q., Wang, X. & Chen, Y.-G. Dishevelled phase separation promotes Wnt
850 signalosome assembly and destruction complex disassembly. *Journal of Cell Biology* **221**
851 (2022). https://doi.org/10.1083/jcb.202205069
852 72 Wang, F. & Zhang, Y. Physiology and pharmacological targeting of phase separation. *J*
853 *Biomed Sci* **31**, 11 (2024). https://doi.org/10.1186/s12929-024-00993-z
854

Figures

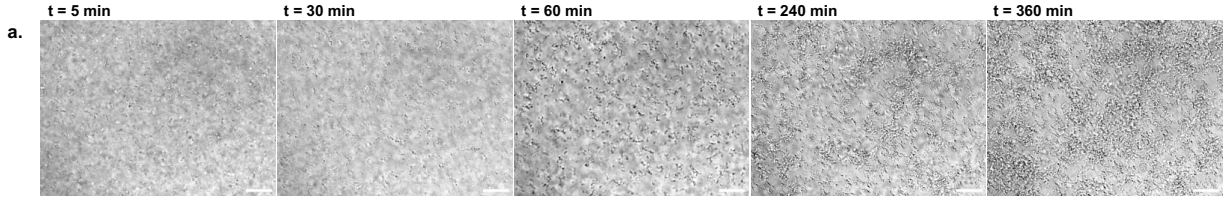
a.
t = 5 min
t = 30 min
t = 60 min
t = 240 min
t = 360 min

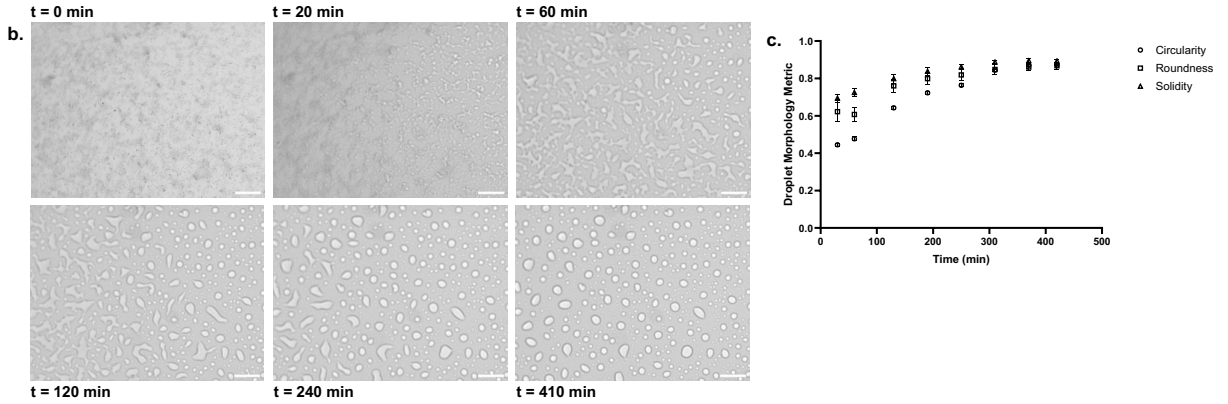
b.
t = 0 min
t = 20 min
t = 60 min
t = 120 min
t = 240 min
t = 410 min
c.
Droplet Morphology Metric
Time (min)
Circularity
Roundness
Solidity

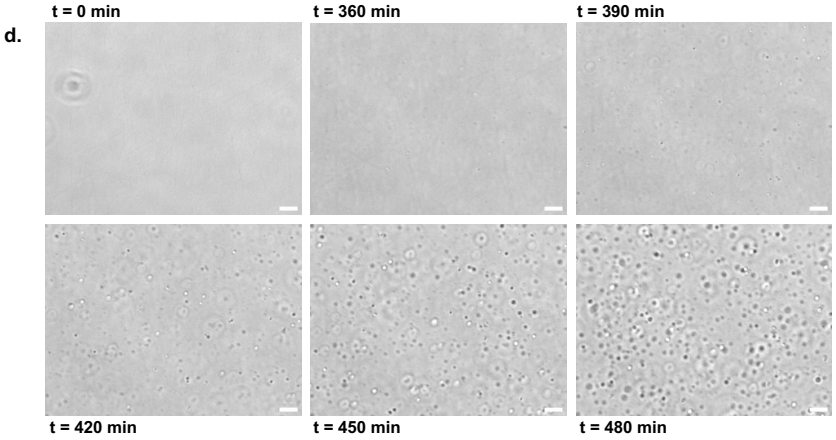
d.
t = 0 min
t = 360 min
t = 390 min
t = 420 min
t = 450 min
t = 480 min

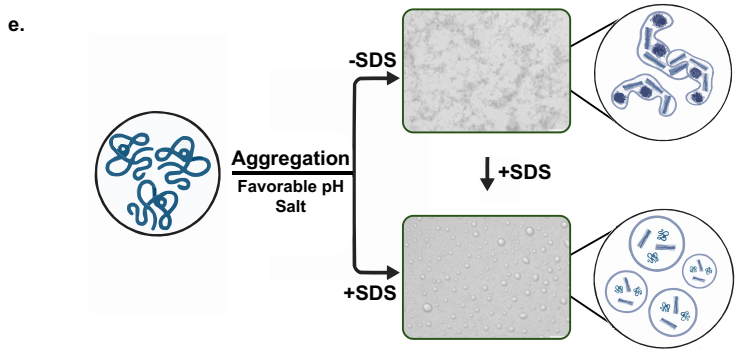
e.
Aggregation
Favorable pH
Salt
-SDS
+SDS
+SDS

881 **Figure 1. Three-phase transition of recombinant full-length TDP-43 induced by charge**
882 **modulation**

883 **a** Gradual formation of solid aggregates from soluble TDP-43 at pH 6 and 0.5 M NaCl. Scale bar
884 is 40μm. **b** Solid aggregates converted into a hydrogel upon addition of SDS (final concentration
885 0.03%), then progressively transformed into spherical droplets over 7 hours. Time notations begin
886 at the addition of SDS. Scale bar is 40μm. **c** The diagram illustrates the time-dependent
887 morphological changes measured by circularity, roundness, and solidity (see Materials and
888 Methods). Error bars are Standard Errors of the Mean. **d** Droplets formed directly from solution
889 following SDS addition, with the most pronounced transition occurring between the 6th and 8th
890 hour. Scale bar is 20μm. **e** Schematic representation showing how TDP-43 can transition among
891 all three phases through controlled induction.

892

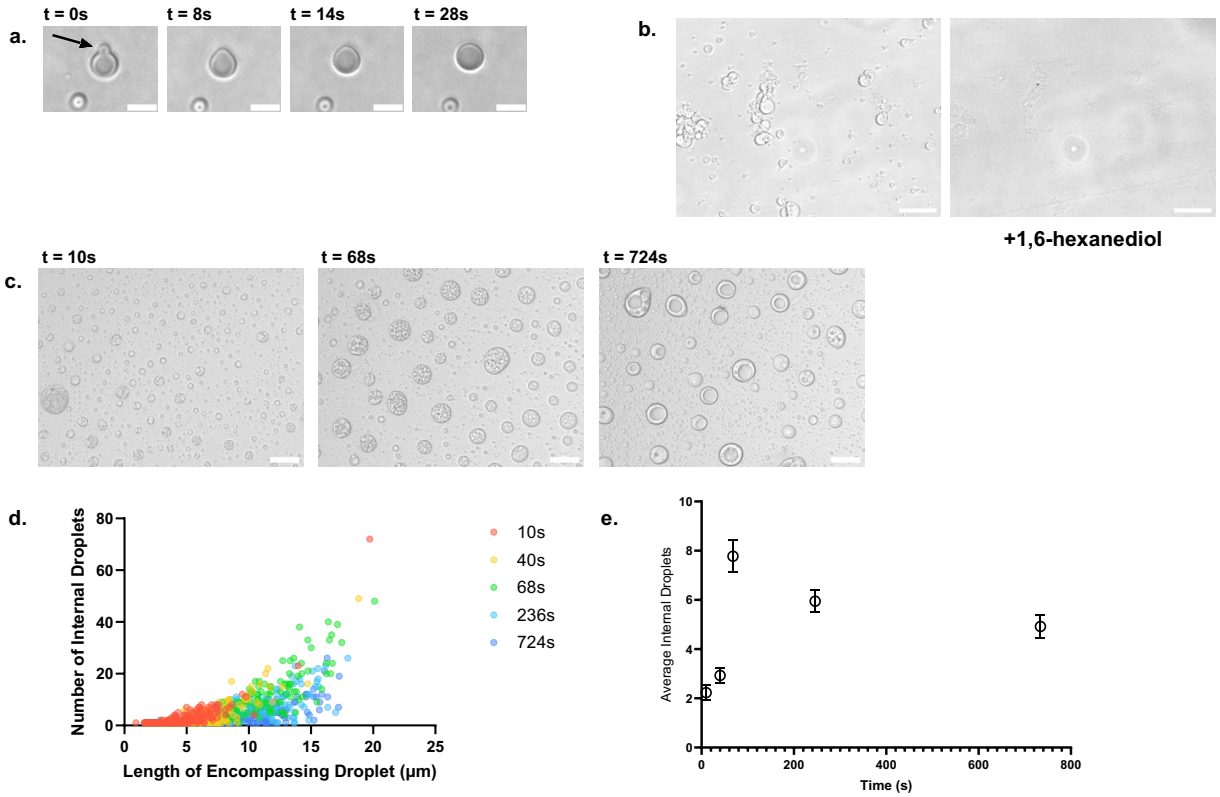

Figure 2. Droplets induced from solid aggregates exhibit liquid-like properties

a Time-lapse images showing a small droplet (arrow) gradually merging with a larger droplet. Scale bar is 10μm. **b** Droplets derived from aggregates dissolve upon treatment with 1,6-hexanediol, consistent with typical LLPS behavior. Scale bar is 40μm. **c** Formation of multi-emulsion droplets upon addition of glycine (50 mM) to initial aggregate-derived droplets. Time indications begin at addition of glycine. Scale bar is 20μm. The transition occurs on the scale of minutes, progressing from small droplets (left) to multiple inner droplets encapsulated within larger outer droplets (middle), and finally to fused, larger droplets (right). **d** Graph showing the number of internal droplets (Y-axis) versus the size of the encompassing droplet (X-axis) and time in seconds (color legend). **e** Graph displaying changes in average number of internal droplets per encompassing droplet (Y-axis) over time in seconds (X-axis). Error bars are Standard Errors of the Mean.

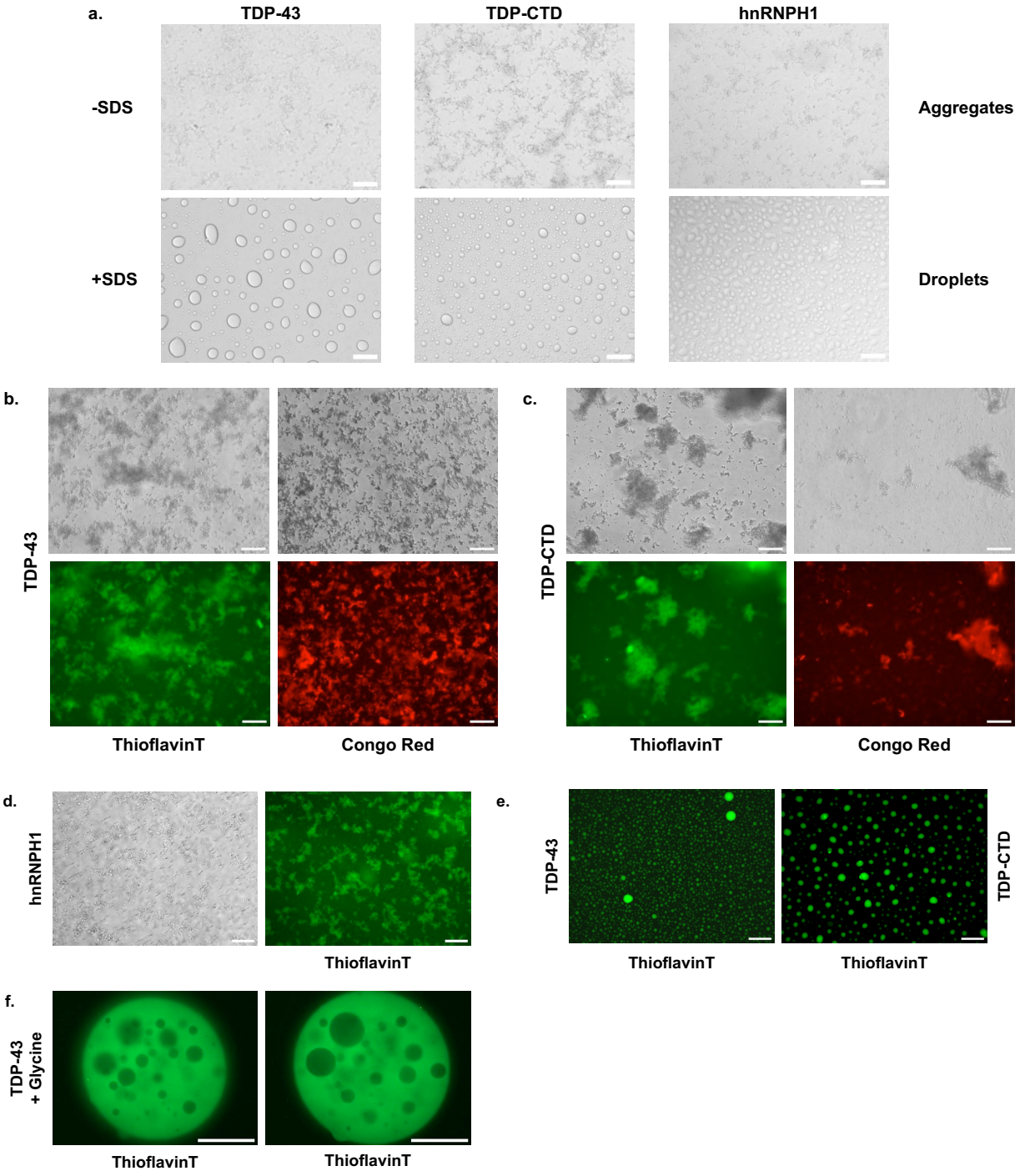

Figure 3. TDP-43, TDP-CTD, and hnRNPH1 form amyloid-positive aggregates and droplets

a Side-by-side comparison of solid aggregates formed by inducing soluble TDP-43, TDP-CTD, and hnRNPH1 at pH 6.0 and 0.5 M NaCl (top), and droplets formed after further addition of SDS to a final concentration of 0.03% (bottom). Images were taken 8 hours after induction. Scale bar

944 is 20μm. **b-d** Aggregates formed by TDP-43 (**b**) and TDP-CTD (**c**) stain positive with ThT and
945 Congo Red (top: bright field; bottom: fluorescence images). **d** hnRNPH1 also stains positive for
946 ThT. Scale bar is 40μm. **e** Representative data showing droplets formed directly from soluble
947 TDP-43 and TDP-CTD solutions exhibit ThT staining. Scale bar is 40μm. **f** Multi-emulsion droplet
948 formed upon addition of glycine (50 mM), with ThT included; shown are confocal fluorescence
949 images from a representative Z-stack acquired using Cytation10 (40×). The z-distance between
950 the two slices is 20μm. Scale bar is 100μm.
951

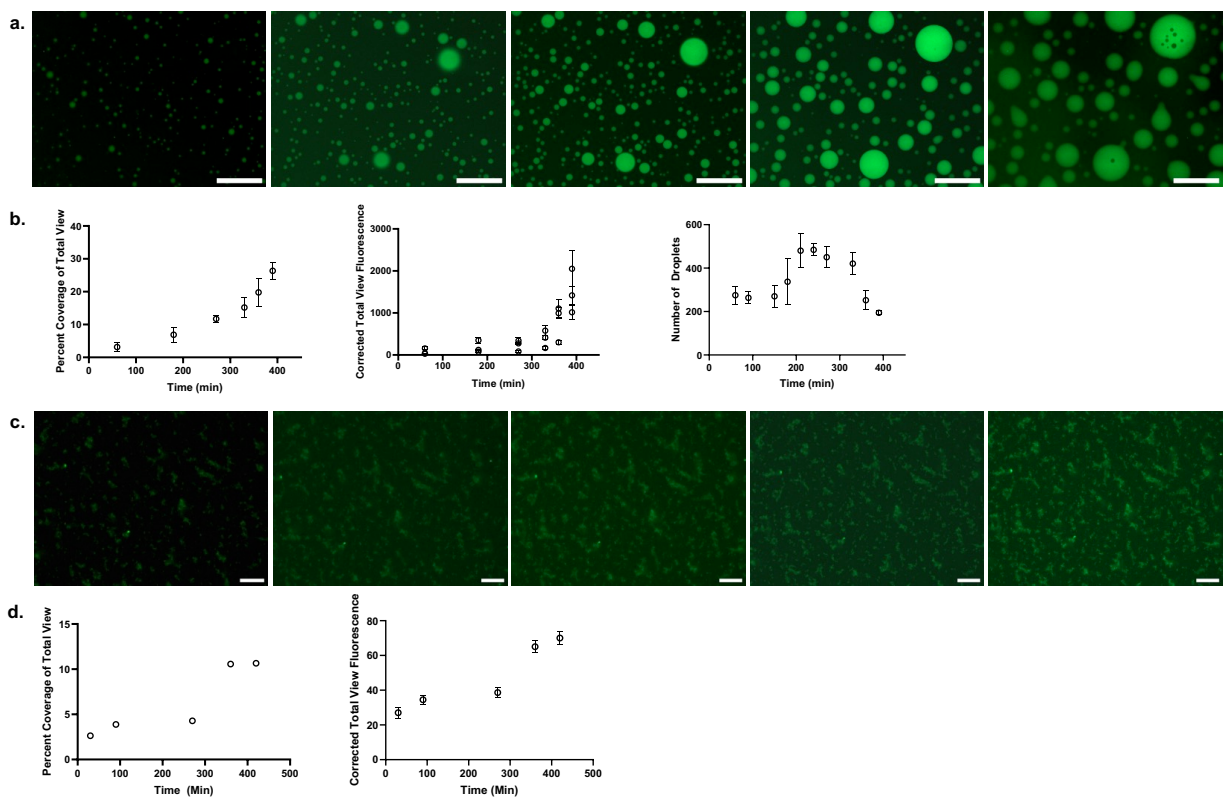

Figure 4. Time course of amyloid-containing droplet and solid aggregate formation

a Still photos taken at indicated time points from a time-lapse series of fluorescence image capturing droplets formed from soluble TDP-43. ThT was added to protein solution before addition of SDS (0.03% final concentration) at time 0. Arrows point to example droplets in the merging process. Scale bar is 100μm. **b** Quantitative analysis of count, percentage of view covered, and Corrected Total View Fluorescence (CTVF) of the droplets formed from 3 separate, non-overlapping views of the same time lapse course. Droplet count and area covered are averaged from the 3 views while CTVF is presented from each time point and view. **c** Still photos taken at indicated time points from a time-lapse series of fluorescence image capturing solid aggregates from soluble solution of TDP-43. ThT was added to protein solution before addition of 1M Tris-HCl pH6 and 5M NaCl at 10% final volume at time 0. Scale bars are 50μm. All reactions were carried out at room temperature, ~25°C. **d** Quantitative analysis of view covered and fluorescence intensity of the solid aggregates formed. Data came from 1 representative view of the time lapse.

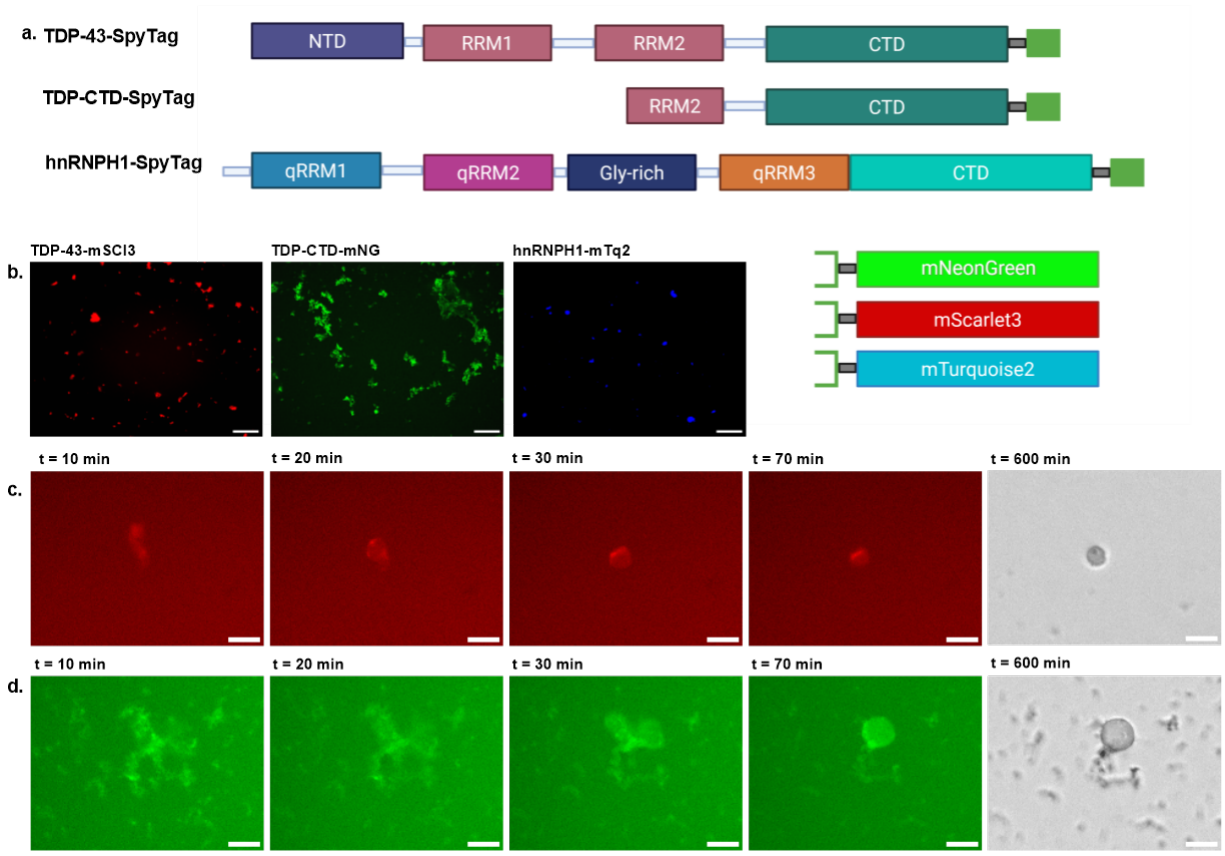

Figure 5. Labeling phase-transition proteins with switchable fluorescent tags

a Schematic representation of protein domains fused with SpyTag/SpyCatcher modules. **b** Solid aggregates formed by TDP-43–mScarlet3 (left), TDP-CTD–mNeonGreen (middle), and hnRNPH1–mTurquoise2 (right) under SDS induction conditions. Scale bar is 40μm. **c, d** Time-lapse images showing TDP-43–mScarlet3 (**c**) and TDP-CTD–mNeonGreen (**d**) transitioning from solid aggregates into droplets; the corresponding bright-field image for the final fluorescence frame is shown on the right. Time notations begin after addition of SDS. Scale bars are 10μm.

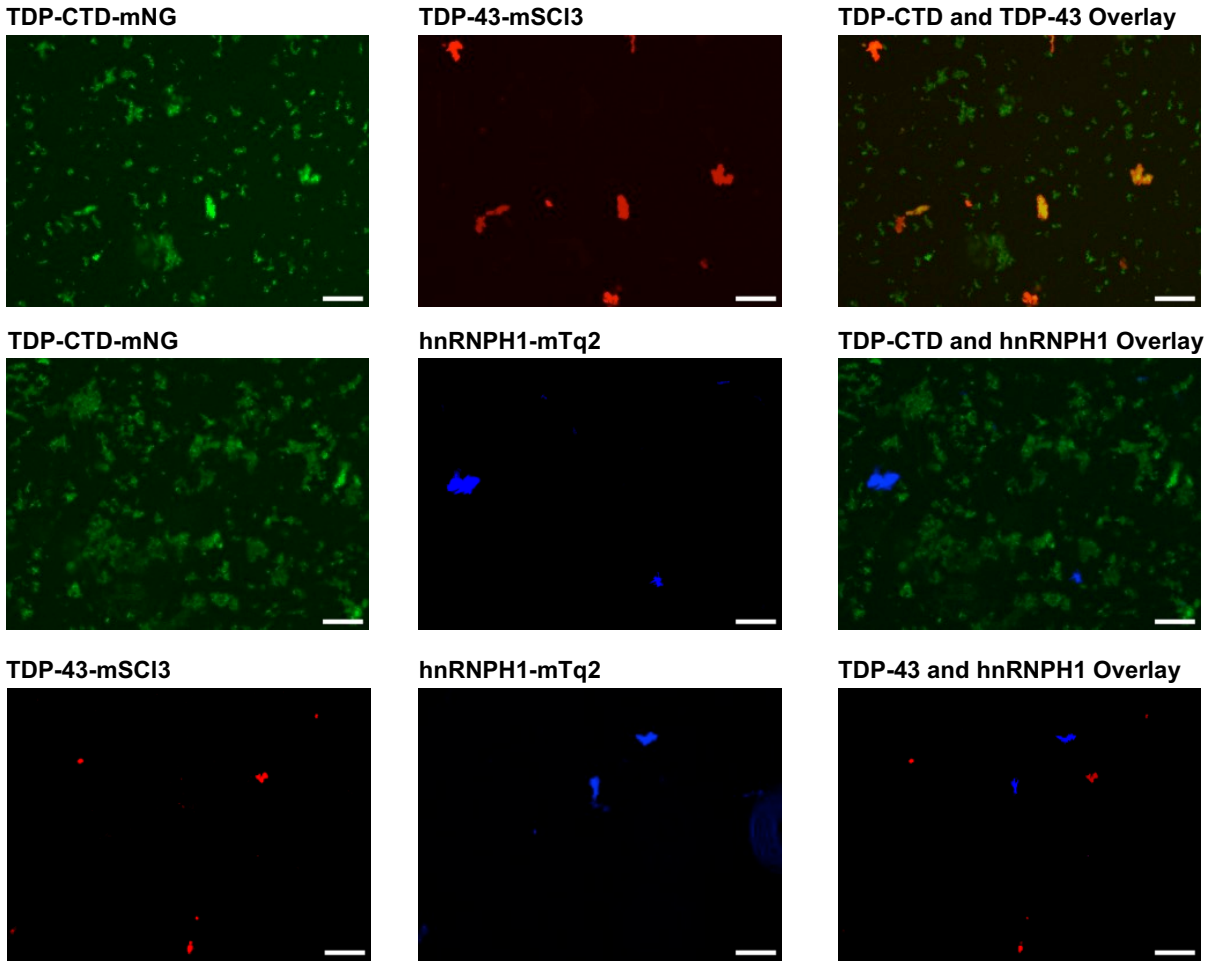

Figure 6. Seeding of phase transition depends on protein compatibility

Pairwise mixing of TDP-CTD–mNeonGreen (mNG), TDP-43–mScarlet3 (mSCI3), and hnRNPH1–mTurquoise2 (mTq2) in solution prior to induction to form aggregates. Coaggregates between TDP-CTD–mNeonGreen and TDP-43–mScarlet3 appear as yellow-orange due to fluorescence overlap. Scale bar is 20μm.